ACS NANO

www.acsnano.org

Functional Metasurface Quarter-Wave Plates for Simultaneous Polarization Conversion and Beam Steering

Yadong Deng, Cuo Wu, Chao Meng, Sergey I. Bozhevolnyi,* and Fei Ding*

Cite This: *ACS Nano* 2021, 15, 18532−18540

Read Online

ACCESS | Metrics & More | Article Recommendations | Supporting Information

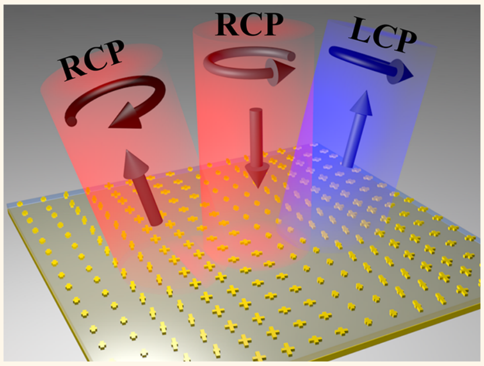

ABSTRACT: **The capability to manipulate the polarization state of light at the nanoscale is of paramount importance in many emerging research areas ranging from optical communication to quantum information processing. Gap-surface plasmon (GSP) metasurfaces, which provide advantages and abilities of molding reflected fields, have been demonstrated excellently suited for integration of multifunctional polarization optics into a single device. Here, we establish a versatile GSP metasurface platform based on nanoscale quarter-wave plates (nano-QWPs) that enable efficient circular-to-linear polarization conversion along with the complete phase control over reflected fields. Capitalizing on the nano-QWP design, we demonstrate, both theoretically and experimentally, how resonance and geometric phases can be used in concert to achieve independent and simultaneous phase modulation of both co- and cross-polarized circularly polarized (CP) waves by realizing arbitrary beam steering of co- and cross-polarized CP channels in a broadband near-infrared range. The GSP metasurface platform established in our work provides versatile and flexible solutions to enrich multiple functionalities for diversified metasurface-based polarization optics exploited in modern integrated photonic devices and systems.**

KEYWORDS: *gap-surface plasmon metasurface, quarter-wave plates, resonance phase, geometric phase, polarization conversion, beam steering*

The capability to control and manipulate the polarization state of light, an inherent and important characteristic of optical radiation, is significantly important for contemporary optical instrumentation. Conventional polarization optical components are typically made up of birefringence materials (e.g., crystals and plastics) that introduce and accumulate the phase retardation between two orthogonally polarized electric fields when light propagates over long distances as compared to its wavelength.[1] As a result, these polarization components are inevitably bulky, intrinsically restricting the possibilities for their miniaturization and integration into photonic systems at the nanoscale.

Optical metasurfaces, two-dimensional artificial nanostructures consisting of dense arrays of meticulously designed meta-atoms, have earned a growing amount of attention owing to their unparalleled capabilities for controlling optical fields with subwavelength spatial resolutions.[2−8] In particular, by judiciously designing anisotropic meta-atoms with specific and distinct responses for light polarized along two orthogonal directions, the phase and polarization of reflected and transmitted (by metasurfaces) light can be efficiently manipulated, thereby substituting conventional bulky polarization optics with planar, compact, and multifunctional metasurface-based polarization optics.[9−38] For example, nanoscale waveplates enabling simultaneous polarization transformation and wavefront shaping have been implemented.[19−35] However, most up-to-date functional metasurface waveplates have been focused on half-wave plates,[19,20,22−29,33−35] where only the cross-polarized light component could be manipulated by the orientation-dependent geometric phase or dimension-dependent resonance/propagation phase. Even though spin-decoupled metasurfaces[21,25,28,29,32−36] exhibit excellent performance, only one functionality can be achieved in the cross-polarized channel for a specific circularly polarized (CP) input. To increase the number of functional channels and thus the information capacity under the CP excitation, it would be

Received: September 29, 2021
Accepted: November 11, 2021
Published: November 15, 2021

https://doi.org/10.1021/acsnano.1c08597

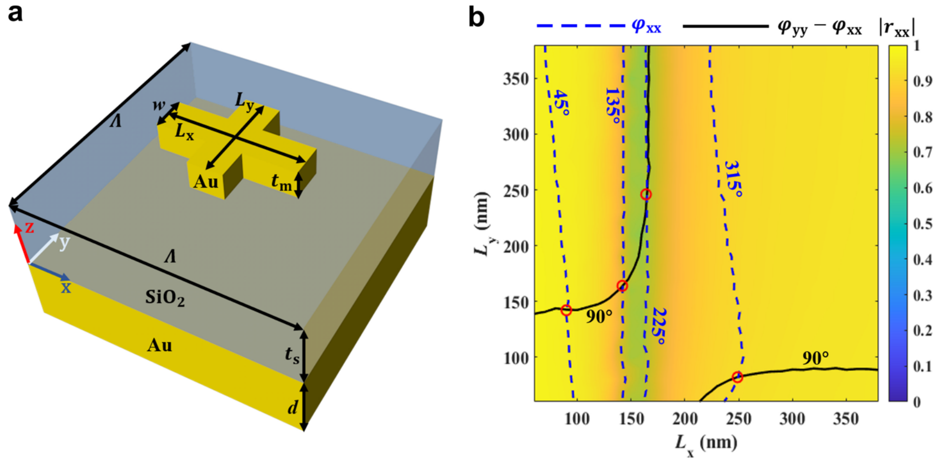

Figure 1. (a) Schematic of the anisotropic MIM meta-atom. (b) Calculated reflection coefficient as a function of the dimensions at the design wavelength of 850 nm for x-polarization. Note the reflection coefficient for y-polarization can be obtained by mirroring the map for x-polarization along the line of $L_x = L_y$. The color map shows the reflection amplitude $|r_{xx}|$, while the blue dashed lines are contours of the reflection phase φ_{xx} with a step of 90° and black solid lines indicate the meta-atoms with the phase difference $\Delta\varphi = \varphi_{yy} - \varphi_{xx}$ equal to 90°.

advantageous to realize similar or different functionalities for both CP waves. Therefore, it is highly desirable to demonstrate metasurface-based quarter-wave plates (QWPs) that utilize and manipulate both co- and cross-polarized output channels simultaneously.[39−42] It is important to note that the QWPs demonstrated thus far are typically operating in the microwave[39−41] or infrared[42] range. Functional nano-QWPs for effective polarization transformation and complete phase modulation are, however, rarely realized in the optical range.

In this paper, we design a set of nano-QWPs based on a gap-surface plasmon (GSP) metasurface configuration, which enable efficient circular-to-linear polarization conversion along with the complete phase control over reflected fields. Capitalizing on the nano-QWP design, we demonstrate how resonance and geometric phases can be complementary utilized to achieve independent and simultaneous phase modulation of both co- and cross-polarized CP waves under CP excitations by realizing arbitrary beam steering of co- and cross-polarized channels in a broadband near-infrared range. Our proposed GSP metasurface platform strengthens the practical applications of metasurfaces with simultaneous phase and polarization manipulation, providing versatile and flexible solutions to implement multifunctional meta-devices at the nanoscale.

RESULTS AND DISCUSSION

QWP Meta-Atom Design. Let us start with the basic principle of realizing metasurface QWPs by considering a birefringent meta-atom with its major axes along x- and y-directions. Generally, the response of such an anisotropic meta-atom could be described by the Jones matrix in the linear polarization basis:

$$J_{\text{linear}} = \begin{pmatrix} r_{xx} & 0 \\ 0 & r_{yy} \end{pmatrix} \tag{1}$$

where $r_{xx} = |r_{xx}|e^{i\varphi_{xx}}$ and $r_{yy} = |r_{yy}|e^{i\varphi_{yy}}$ are the reflection coefficients under x- and y-polarized excitations, which are mainly determined by the dimensions of the birefringent meta-atom along its two main axes. Once the reflection amplitudes are equal (i.e., $|r_{xx}| = |r_{yy}|$) and the relative phase difference $\Delta\varphi = \varphi_{yy} - \varphi_{xx}$ is ±90°, the birefringent meta-atom functions as a nano-QWP. If the nano-QWP with $\Delta\varphi = 90°$ is rotated by an angle of θ with respect to the x-axis, the corresponding Jones matrix can be written as

$$J(\theta) = |r_{xx}|e^{i\varphi_{xx}}M^{-1}(\theta)\begin{pmatrix} 1 & 0 \\ 0 & i \end{pmatrix}M(\theta) \tag{2}$$

where $M(\theta) = \begin{pmatrix} \cos\theta & \sin\theta \\ -\sin\theta & \cos\theta \end{pmatrix}$ represents the rotation matrix. For the right-handed circularly polarized (RCP) incident light with $E_{\text{in}} = \frac{1}{\sqrt{2}}\begin{pmatrix} 1 \\ -i \end{pmatrix}$, the output field becomes linearly polarized (LP) and the angle of linear polarization (AoLP) is $\theta + \pi/4$

$$E_{\text{out}} = |r_{xx}|e^{i\varphi_{xx}}e^{-i\theta}\begin{pmatrix} \cos\left(\theta + \frac{\pi}{4}\right) \\ \sin\left(\theta + \frac{\pi}{4}\right) \end{pmatrix} \tag{3}$$

Additionally, the LP light gains an additional phase modulation of $\varphi_{xx} - \theta$. Meanwhile, the LP light can be decomposed into two CP components in the circular polarization basis, which is written as

$$E_{\text{out}} = \frac{1}{2}|r_{xx}|e^{i\left(\varphi_{xx}+\frac{\pi}{4}\right)}\begin{pmatrix} 1 \\ -i \end{pmatrix} + \frac{1}{2}|r_{xx}|e^{i\left(\varphi_{xx}-\frac{\pi}{4}\right)}e^{-i2\theta}\begin{pmatrix} 1 \\ i \end{pmatrix} \tag{4}$$

Equation 4 indicates that the reflected field contains two components; where the first part stands for the copolarized reflective wave that maintains the same helicity as the incident RCP wave, whereas the second part is the cross-polarized wave with the reversed helicity [i.e., left-handed circularly polarized (LCP)]. Here we define the copolarized and cross-polarized reflection coefficients as $r_{\text{co}} = \frac{\sqrt{2}}{2}|r_{xx}|e^{i\left(\varphi_{xx}+\frac{\pi}{4}\right)}$ and $r_{\text{cr}} = \frac{\sqrt{2}}{2}|r_{xx}|e^{i\left(\varphi_{xx}-\frac{\pi}{4}-2\theta\right)}$ in the circular polarization basis, respectively. Thus, the phase of the copolarized CP beam $\varphi_{\text{co}} = \varphi_{xx} + \pi/4$ is only associated with the resonance phase, while cross-polarized CP phase distribution $\varphi_{\text{cr}} = \varphi_{xx} - \pi/4 - 2\theta$ is determined by both resonance and geometric phases, which depends on the meta-atom's dimensions and orienta-

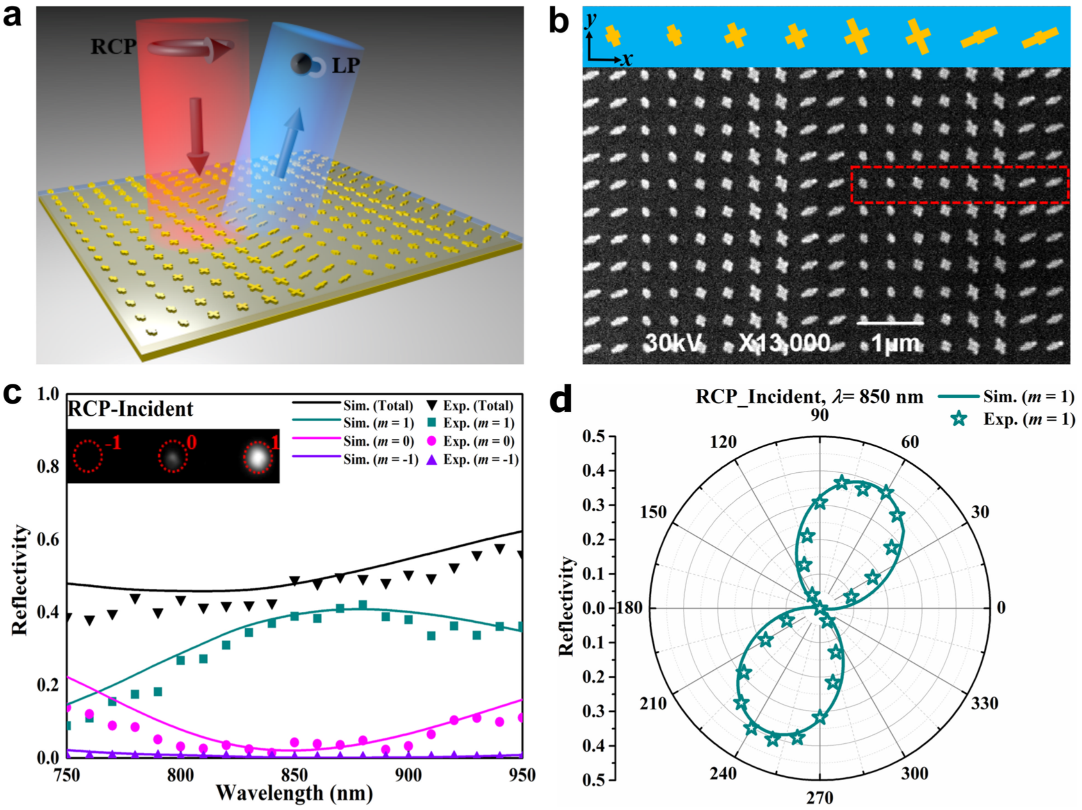

Figure 2. (a) Schematic of the GSP gradient MS1 for circular-to-linear polarization conversion and beam steering under RCP excitation. (b) SEM image of the fabricated MS1. The inset shows the layout of one MS1 supercell with each meta-atom rotated by an angle of 22.5° with respect to the *x*-axis along the counterclockwise direction. (c) Simulated (solid lines) and experimental (markers) diffraction efficiencies of different orders as a function of wavelength for RCP incident light. The inset shows the optical image of the diffraction spots at the wavelength of 850 nm. (d) Simulated (dark cyan solid line) and experimental (dark cyan star markers) polarization state diagrams of the steered beam within +1 diffraction order for RCP incident light at the wavelength of 850 nm.

tions, respectively. As a result, the co- and cross-polarized CP channels can be dependently or independently manipulated.

To design the anisotropic meta-atom that functions as a nano-QWP, we use a typical metal−insulator−metal (MIM) GSP resonator[43] as the fundamental building block. As shown in Figure 1a, the MIM unit cell consists of a gold (Au) cross-shaped nanoantenna, a silicon dioxide (SiO_2) spacer layer, and a continuous Au film. The periodicity of designed MIM unit cells is $\Lambda = 400$ nm, which is much smaller than the design wavelength of $\lambda = 850$ nm to eliminate the high-order diffraction. The thickness of the middle SiO_2 spacer layer is optimized to $t_s = 100$ nm, ensuring high reflection efficiency and sufficient resonance phase coverage. The thickness and width of topmost Au antennas are $t_m = 40$ nm and $w = 50$ nm, respectively, while the lengths (i.e., L_x and L_y) of the two rectangle constituent bars are varied. The thickness of the bottom Au layer is $d = 100$ nm, which is thick enough to block light transmission. We implemented three-dimensional (3D) full-wave simulations with the commercially available software Comsol Multiphysics (version 5.5) to calculate the complex reflection coefficients of the meta-atoms under *x*- or *y*-polarized incident light. In the simulation, L_x and L_y are varied while other geometrical parameters are kept constant. The relative permittivity of Au is described by the Drude model fitted with the experimental data,[44] and SiO_2 is taken as a lossless material with a constant refractive index of 1.45. An air domain is added above the meta-atom and truncated with a perfectly matched layer to minimize any reflection. An *x*- or *y*-polarized plane wave is normally impinging on the MIM unit cell with periodic boundary conditions employed in both *x*- and *y*-directions. Figure 1b shows the calculated reflection coefficient of the meta-atom with varying L_x and L_y at the targeted wavelength of $\lambda = 850$ nm under *x*-polarized excitation, where nano-QWP candidates with $\Delta\varphi$ matched to 90° are marked with black solid lines. Meanwhile, the available resonance phase of nano-QWPs (i.e., φ_{xx}) can cover a wide range up to 300°. To maintain broad operation bandwidth and high efficiency, four nano-QWPs (red circles) with a phase step of $\Delta\varphi_{xx} = 90°$ are selected to comprise a meta-atom library, which enables simultaneous circular-to-linear polarization conversion and potential wavefront shaping. The geometric parameters and corresponding serial numbers of selected nano-QWPs are shown in Table S1. As a final comment, it is worth noting that the amplitudes of these four nano-QWPs are not perfectly equal, which may slightly affect the performance. To increase the reflection amplitudes of selected (poorly reflecting) meta-atoms, their widths can be propitiously designed (Figures S1 and S2, and Table S3 in the Supporting Information).

Gradient Metasurfaces for Broadband Circular-to-Linear Polarization Conversion and Beam Steering. After designing the four nano-QWPs, we first design gradient metasurfaces that enable simultaneous circular-to-linear polarization conversion and beam steering under LCP and RCP incident light. In this case, the co- and cross-polarized CP channels are molded only by the resonance phase and thus

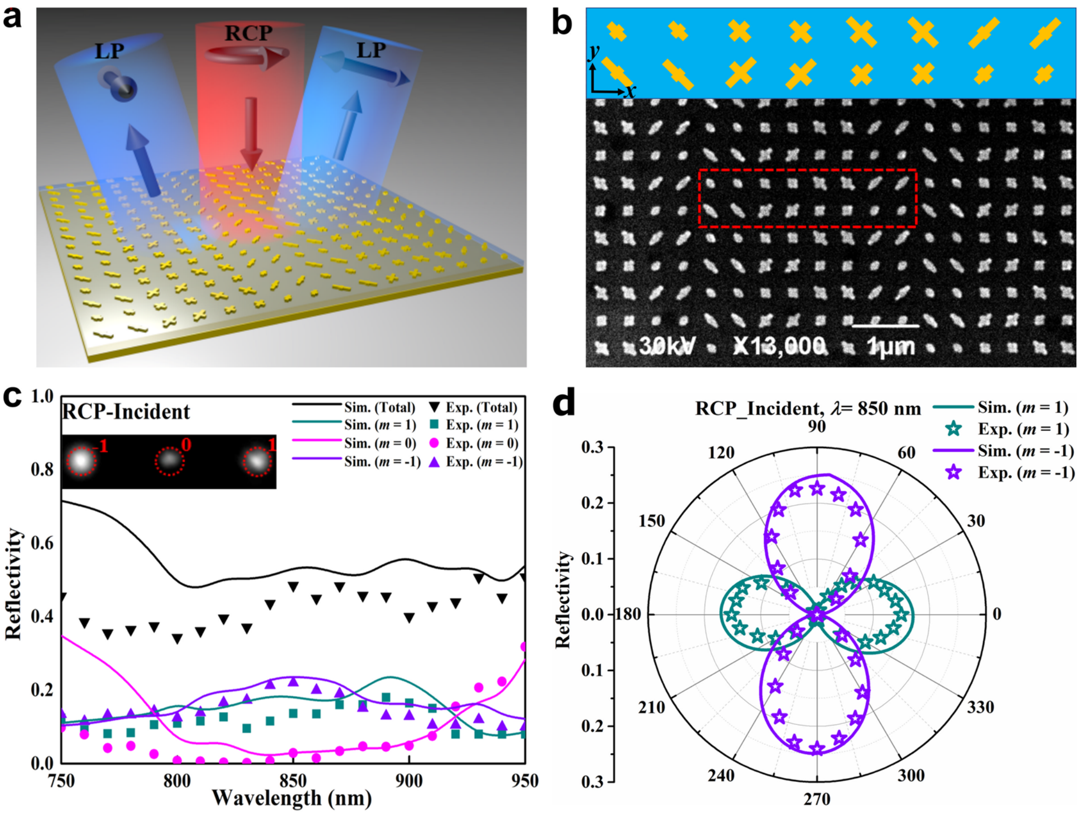

Figure 3. (a) Schematic of the GSP gradient MS2 for generating two spatially separated LP beams with different AoLPs under RCP excitation. (b) SEM image of the fabricated MS2. The inset shows the layout of one MS2 supercell with each nano-QWP rotated by 45° or 135° along the counterclockwise direction in the first and second rows, respectively. (c) Simulated (solid lines) and experimental (markers) diffraction efficiencies of different orders as a function of wavelength for RCP incident light. The inset shows the optical image of the diffraction spots at the wavelength of 850 nm. (d) Simulated (dark cyan/violet solid line) and experimental (dark cyan/violet star markers) polarization state diagrams of the steered beam within ±1 diffraction orders for RCP incident light at the wavelength of 850 nm.

steered to the same direction. Specifically, the meta-atoms comprising the metasurface supercell are all rotated with the same angle of θ_{LP0}. Therefore, the corresponding phase gradient along the x-direction is given as

$$\frac{d\varphi_{\mathrm{LP}}}{dx}=\frac{\partial(\varphi_{xx}(x,y)+\theta_{\mathrm{LP0}})}{\partial x}=\frac{\Delta\varphi_{xx}}{N\cdot\Lambda}=m_{\mathrm{LP}}\cdot\frac{2\pi}{\wedge_{\mathrm{sc}}}\tag{5}$$

where (x, y) indicates the coordinate of each meta-atom, N is the number of identical meta-atoms duplicated in a supercell, m_{LP} represents the diffraction order for the LP reflection field, and $\wedge_{\mathrm{sc}}$ represents the total period of one supercell. Figure 2a schematically illustrates the working principle of the first gradient metasurface (MS1) that converts and steers the CP (e.g., RCP) incident light into an LP wave with a spin-determined AoLP within +1 diffraction order. As shown in Figure 2b, MS1 is made up of four selected nano-QWPs that are all duplicated to make an 8-element supercell to enlarge the periodicity along the x-direction, thereby decreasing the diffraction angle of the steered light within the collection angle of the objective. Within the supercell, each meta-atom is rotated with an angle of $\theta_{\mathrm{LP0}} = 22.5°$ with respect to the x-axis along the counterclockwise direction. As such, each meta-atom will convert the RCP (LCP) incident light to a secondary LP wave with a fixed AoLP of 67.5° (−22.5°). Additionally, the secondary LP wave gain a linear phase gradient along the x-axis, thereby forming the reflected LP light in +1 diffraction order.

To validate the performance, we first simulated the MS1 supercell and plotted the calculated diffraction efficiencies (solid lines in Figure 2c) of different orders from $m = -1$ to +1 as a function of wavelength for RCP incident light. It is worth noting that the damping rate of Au here is increased by a factor of 3 to account for additional losses in terms of surface scattering, grain boundary effects, and increased damping related to the 3 nm titanium (Ti) adhesion layer between Au and $\mathrm{SiO_2}$ layers. As expected, the total reflectivity is restricted to 48% because of the increased ohmic loss, and the incident light is exclusively reflected into +1 diffraction order with a theoretical reflectivity of ∼40% at the design wavelength of 850 nm under RCP incident light; however, the other diffraction orders are strongly suppressed. In addition, the simulated polarization state diagram (dark cyan solid line in Figure 2d) of the steered beam within +1 diffraction order indicates the excellent circular-to-linear polarization conversion at the wavelength of 850 nm, with the degree of linear polarization (DoLP) approaching 99.19%. After full-wave simulations, the designed MS1 was fabricated using the standard thin-film deposition, electron beam lithography, and lift-off techniques (see the Methods section for details). The scanning electron microscopy (SEM) image of MS1 is shown in Figure 2b, whose overall size is around 20 × 20 $\mu\mathrm{m}^2$. Generally, the fabricated sample well replicates the designed meta-atoms in terms of shapes and dimensions despite the surface roughness and rounded corners. After fabrication, the sample was characterized using a custom-built optical setup shown in

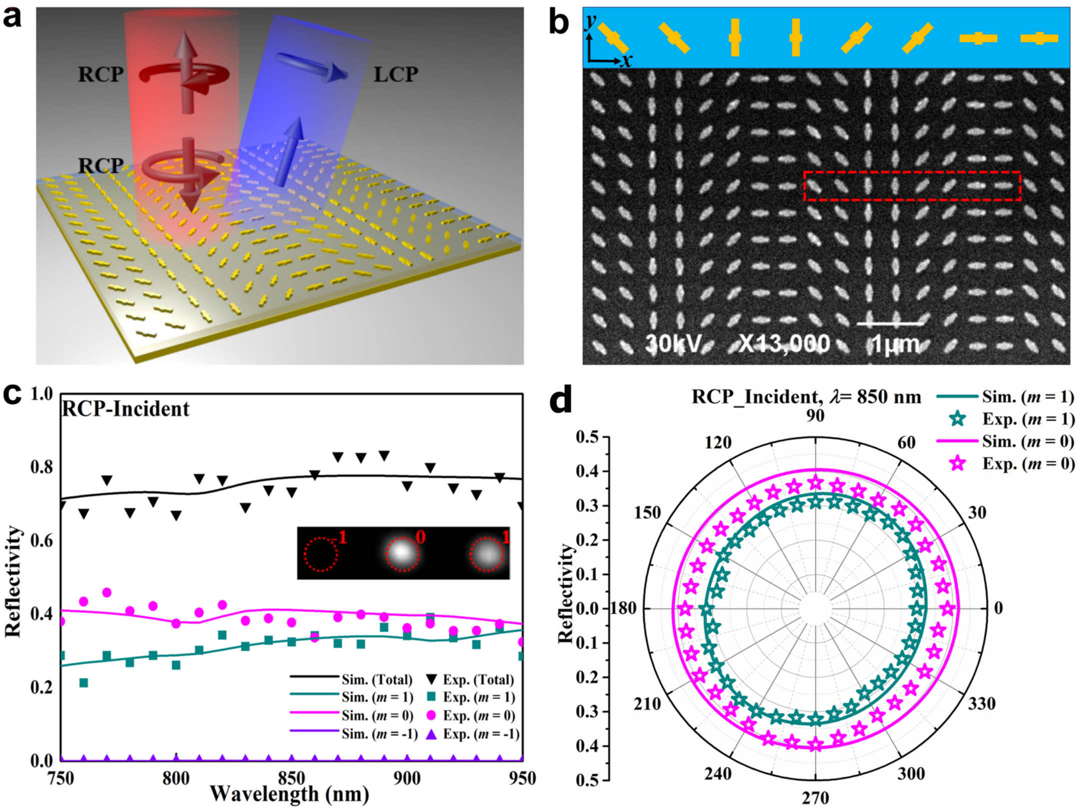

Figure 4. (a) Schematic of the GSP gradient MS3 composed of identical meta-atoms with different rotation angles for steering of co- and cross-polarized CP waves to 0 and +1 diffraction orders. (b) SEM image of the fabricated MS3. The inset shows the layout of one MS3 supercell composed of identical meta-atoms with different rotation angles. (c) Simulated (solid lines) and experimental (markers) diffraction efficiencies of different orders as a function of wavelength for RCP incident light. The inset shows the optical image of the diffraction spots at the wavelength of 850 nm. (d) Simulated (dark cyan/magenta solid line) and experimental (dark cyan/magenta star markers) polarization state diagrams of the steered beams within 0 and +1 diffraction orders for RCP incident light at the wavelength of 850 nm.

Figure S4. From the optical image of the diffraction spots in the inset of Figure 2c, we could see that almost all the incident light has been reflected into +1 diffraction order, demonstrating the excellent capability of beam steering. The performance of our fabricated MS1 was further measured by determining the corresponding diffraction efficiency in each order. As displayed in Figure 2c, in general, the simulated and experimental diffraction efficiencies coincide fairly well. Specifically, the total reflectivity is close to 50% and the diffraction efficiency of +1 order is ~40% at $\lambda = 850$ nm under RCP incident light in the experiment. The measured (dark cyan star markers) reflectance as a function of the orientation of the analyzer in front of the CCD camera for +1 diffraction order under RCP excitation also presents great consistency with the simulation result at the design wavelength of 850 nm, as shown in Figure 2d. In particular, the measured DoLP is 99.42%. Meanwhile, the MS1 enables efficient circular-to-linear polarization conversion and beam steering in a broadband spectrum ranging from 800 to 900 nm (Figure S5). Once the incident light is switched to LCP, an LP beam with the AoLP of −22.5° is generated and routed to +1 diffraction order (Figure S6).

In addition to producing a single LP beam in the desired direction under a CP excitation, it is interesting to simultaneously generate more LP beams with different AoLPs in spatially separated channels. Therefore, we design a second GSP metasurface (MS2) capable of converting the incident CP beam into two LP beams with orthogonal linear polarization states in the opposite directions (Figure 3a) by interweaving two metasurface subsupercells along the y-direction, where nano-QWPs are rotated by 45° or 135° along the counterclockwise direction in the first and second rows, respectively (Figure 3b). In particular, MS2 can convert the RCP incident beam into x- and y-polarized waves into respective ±1 diffraction orders. Once the incident light is switched to LCP, the reflected beams within ±1 diffraction orders become y- and x-polarized. The calculated diffraction efficiencies of MS2 as a function of wavelength for RCP incident light are shown in Figure 3c, which indicate a broadband response from 800 to 900 nm. Compared with MS1, the zero-order diffraction slightly increases, which may be ascribed to the enlarged periodicity of $2\Lambda = 800$ nm between identical subsupercells along the y-direction, leaving away from the criterion of true subwavelength separation and thus degrading the performance of individual metasurfaces. Despite the disturbance, the desired reflectivities within ±1 diffraction orders are both ~20% with the zero-order diffraction efficiency below 5% at the design wavelength of 850 nm. Analogously, we fabricated and characterized the sample MS2 using the same processes. Figure 3b shows the SEM image of the fabricated sample MS2 whose overall size is also about 20×20 μm^2. From the optical image of the diffraction spots in Figure 3c, we could observe that most of the energy has been reflected to ±1 diffraction orders, manifesting the desired beam steering capability at the design wavelength of 850 nm. Additionally, there is a reasonable

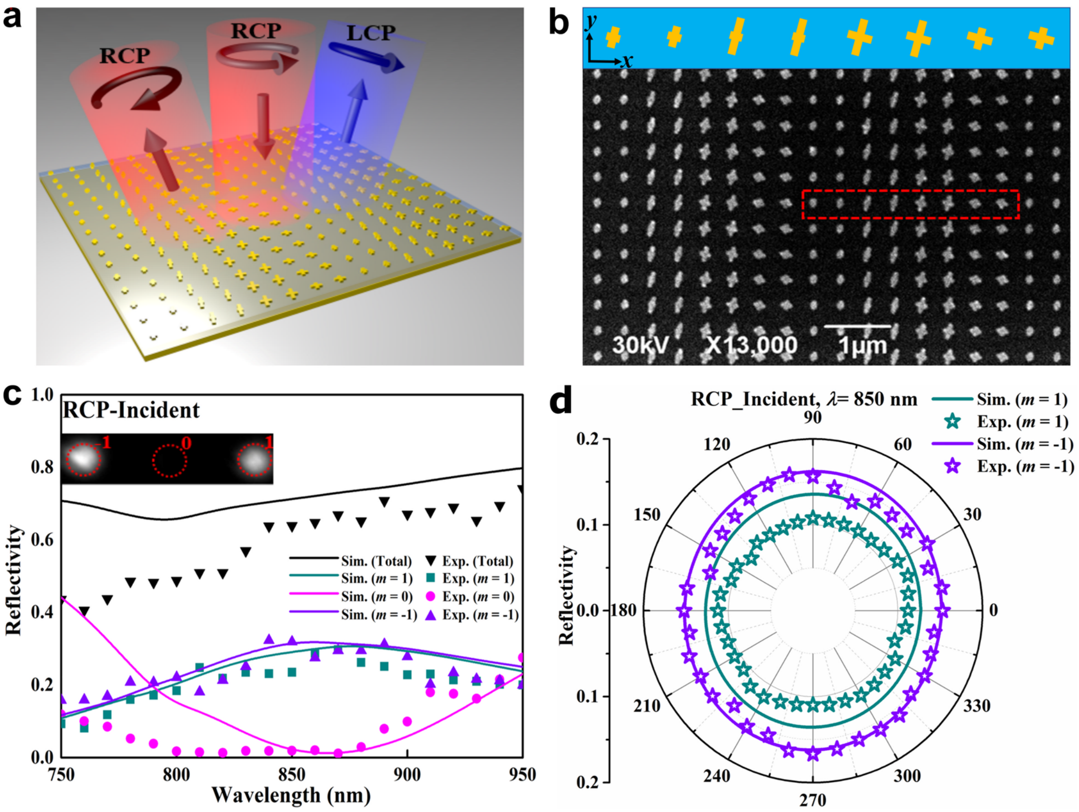

Figure 5. (a) Schematic of the GSP gradient MS4 composed of meta-atoms with different dimensions and rotation angles for steering of co- and cross-polarized CP waves to −1 and +1 diffraction orders. (b) SEM image of the fabricated MS4. The inset shows the layout of one MS4 supercell composed of meta-atoms with different dimensions and rotation angles. (c) Simulated (solid lines) and experimental (markers) diffraction efficiencies of different orders as a function of wavelength for RCP incident light. The inset shows the optical image of the diffraction spots at the wavelength of 850 nm. (d) Simulated (dark cyan/violet solid line) and experimental (dark cyan/violet star markers) polarization state diagrams of the steered beam within −1 and +1 diffraction orders for RCP incident light at the wavelength of 850 nm.

agreement between the simulated and experimental efficiencies of different orders at $\lambda = 850$ nm (simulation: ~3.00%, ~18.20% and ~23.70% for the diffraction orders of $m = 0$ and ±1, respectively; experiment: ~ 2.90%, ~13.60% and ~22.00% for the diffraction orders of $m = 0$ and ±1, respectively). Moreover, the similar simulated (dark cyan/violet solid line) and experimental (dark cyan/violet star markers) polarization state diagram as a function of the orientation of the analyzer under RCP excitation at the design wavelength of 850 nm could be observed in Figure 3d. Importantly, the measured DoLPs are as high as 99.54% and 99.36% for the diffraction orders of $m = \pm 1$. The MS2 sample also exhibits reasonably good performance at other wavelengths and the measurements only show tiny inconsistency with simulations (Figure S7), a feature that we attribute to imperfections in the manufactured metasurface and some deviation during the measurement process. Similarly, the MS2 sample could operate equally well in the case of LCP incidence (Figure S8).

Gradient Metasurfaces for Independent Beam Steering of Co- and Cross-Polarized CP Waves. As shown in eq 4, the designed nano-QWPs enable simultaneous and independent phase modulation of co- and cross-polarized reflected waves in the circular polarization basis by employing the resonance and geometric phases at the same time. Specifically, the copolarized output channel gains a phase term of $\varphi_{co} = \varphi_{xx} + \pi/4$ imposed by the dimension-varied meta-atoms while the cross-polarized counterpart carries a phase shift of $\varphi_{cr} = \varphi_{xx} - \pi/4 - 2\theta$ determined by the dimensions and orientations of meta-atoms for the RCP incident light. Since the selected meta-atoms function as nano-QWPs, the co- and cross-polarized channels share equal output energy. To validate the versatility and capability of independent beam steering in two orthogonal CP channels, we now design two gradient metasurfaces (MS3 and MS4) that can steer the reflected CP beams into spatially separated channels. As such, the corresponding phase gradients that allow to steer CP output channels are

$$\frac{d\varphi_{co}}{dx} = \frac{\partial\left(\varphi_{xx}(x, y) + \frac{\pi}{4}\right)}{\partial x} = \frac{\Delta\varphi_{xx}}{N\cdot\Lambda} = m_{co}\cdot\frac{2\pi}{\Lambda_{sc}} \tag{6}$$

$$\frac{d\varphi_{cr}}{dx} = \frac{\partial\left(\varphi_{xx}(x, y) - \frac{\pi}{4} - 2\cdot\theta(x, y)\right)}{\partial x} = \frac{\Delta\varphi_{xx} - 2\cdot\Delta\theta}{N\cdot\Lambda} = m_{cross}\cdot\frac{2\pi}{\Lambda_{sc}} \tag{7}$$

where $\theta(x, y)$ is the rotated angle of each meta-atom, $\Delta\theta$ is the relative angle between two differently sized meta-atoms, m_{co} and m_{cross} represent the respective diffraction orders for co- and cross-polarized reflection fields, respectively. For MS3, it will reflect RCP incident light to copolarized (RCP) and cross-polarized (LCP) channels toward the 0 and +1 diffraction orders, respectively, as shown in Figure 4a. By substituting $m_{co} = 0$, $m_{cross} = 1$, and $N = 2$ into the above equations, we get the solutions of $\Delta\varphi_{xx} = 0$ and $\Delta\theta = -\pi/4$ with a metasurface supercell composed of 8 elements. Therefore, we only need to choose one nano-QWP from our meta-atom library and rotate each meta-atom accordingly to fulfill the geometric phase requirements. Considering the reflection efficiency, meta-atom No.4 is selected and distributed to make a supercell, where meta-atoms are rotated with angles $\theta(x, y)$ of −45°, −45°, −90°, −90°, −135°, −135°, −180°, and −180°, respectively (Figure 4b). Such a design could be constructed by sequentially placing the 8 elements with a center-to-center distance of Λ = 400 nm and subsequently decrease the first-order diffraction angle to 15.4°. As expected, almost all the incident RCP light is reflected into 0 and +1 diffraction orders and −1 diffraction order is strongly suppressed (approaching 0) in a wider spectrum range from 750 to 950 nm (Figure 4c), which is ascribed to the broadband nature of the geometric phase. Compared with MS1 and MS2, MS3 features a higher total reflectivity since only one highly efficient nano-QWP is involved. At the design wavelength of 850 nm, the reflected electric fields at two orthogonal CP states assemble well-defined wavefronts (Figure S9a,c). Based on the same setup, the diffraction efficiency of each order can be resolved in the investigated spectrum range. Overall, reasonable agreement is observed between the measured and calculated diffraction efficiencies, verifying the broadband beam steering for both co- and cross-polarized CP light. Specifically, the measured diffraction efficiencies of 0 and +1 orders are ~37% and ~32%, respectively, at the design wavelength of 850 nm, which is clearly seen from the optical image of two bright diffraction spots in Figure 4c. After validating the capability of steering CP waves in two spatially separated channels, it is important to verify their polarization states. As such, we plot the simulated (dark cyan/magenta solid line) and experimental (dark cyan/magenta star markers) polarization state diagram as a function of the orientation of the analyzer for 0 and +1 diffraction orders at λ = 850 nm in Figure 4d. In general, the measured polarization diagrams well assemble circular shapes with the degrees of circular polarization (DoCPs) above 93.70% and −92.40% for the diffraction orders of $m = 0$ and 1, respectively, which are consistent with the simulated values of 99.60% and −99.30%. More simulated and experimental results at other incident wavelengths under RCP excitation are shown in Figure S9b,d.

As a more general case, MS4 can steer the reflected co- and cross-polarized CP waves into −1 and +1 diffraction orders, respectively (Figure 5a). Thus, we substitute $m_{\text{co}} = -1$, $m_{\text{cross}} = 1$, and $N = 2$ into eqs 6 and (7) and select four nano-QWPs with different dimensions and rotation angles to form an 8-element supercell, which provides resonance and geometric phases simultaneously. As shown in the inset of Figure 5b, the 8 elements are distributed in a certain order (i.e., meta-atoms No.1, No.1, No.4, No.4, No.3, No.3, No.2, and No.2) and the corresponding rotation angles $\theta(x, y)$ are −15°, −15°, 75°, 75°, 165°, 165°, 255°, and 255°, respectively. Illuminating MS4 with an RCP wave at normal incidence, we measured diffraction efficiencies of orders $|m| \leq 1$, as shown in Figure 5c. In general, reasonable agreement is observed between the measured and calculated diffraction efficiencies, verifying the desired steering capability, albeit with some discrepancies regarding the zero-order diffraction, particularly at short wavelengths. Compared with MS3 composed of spatially oriented identical meta-atoms to supply geometric phase, MS4 can only work in a narrower bandwidth since more meta-atoms are involved and each meta-atom has its individual operating bandwidth. At the design wavelength of 850 nm, the experimental diffraction efficiencies for −1 and +1 orders are found to be ~32.00% and ~23.50%, respectively (Figure 5c). In addition, the simulated (dark cyan/violet solid line) and experimental (dark cyan/violet star markers) polarization state diagrams are in good agreement with each other at λ = 850 nm, as shown in Figure 5d. Quantitatively, the measured DoCPs are around 90.30% and −92.00%, indicating that co- and cross-polarized CP waves have been successfully steered into −1 and +1 diffraction orders, respectively. As expected, the reflected electric fields at two orthogonal CP states exhibit tilted planar wavefronts (Figure S10a,c). The simulated and experimental results at wavelengths of 800 and 900 nm under RCP incident light could be seen in Figure S10b,d, validating the broadband nature of the implemented MS4.

CONCLUSIONS

In this paper, we have demonstrated a set of GSP nano-QWPs for efficient circular-to-linear polarization conversion along with the complete phase control over reflected fields. Based on the nano-QWP design, we have achieved independent and simultaneous phase modulation of both co- and cross-polarized CP waves under CP excitations by realizing arbitrary beam steering of co- and cross-polarized CP channels in the broadband near-infrared range. Specifically, we experimentally demonstrated two GSP gradient metasurfaces (MS1 and MS2) that employ only the resonance phase for efficient circular-to-linear polarization conversion and beam steering of two CP channels in the same direction. In addition, independent beam steering of co- and cross-polarized CP channels in separated channels has been further implemented with MS3 and MS4 that utilize the geometric phase modulation. As an additional comment, we want to emphasize that the efficiencies of considered metasurfaces could further be enhanced by employing differently wide nano-QWPs allowing for larger reflection amplitudes (Figure S2b) and/or using single-crystalline Au with lower absorption in the metasurface fabrication to reduce the metasurface damping (Figure S11). Finally, we would like to emphasize that the designed four GSP metasurfaces operate equally well in the case of the LP excitation (Table S4), which could further enrich the applications. The proposed versatile GSP nano-QWP platform established here strengthens the practical applications of multifunctional integrated metasurfaces with simultaneous phase and polarization manipulation, which can be combined with amplitude manipulation to further extend the information capacity.[45,46]

METHODS

Fabrication. All the samples were fabricated by employing the standard thin-film deposition, electron-beam lithography, and lift-off techniques. First, a 3 nm Ti layer, a 100 nm Au layer, and a 1 nm Ti layer were deposited onto a silicon substrate through thermal evaporation successively. Then, a 100 nm SiO_2 spacer layer was deposited with RF-sputtering. Next, a 100 nm PMMA (2% in anisole, Micro Chem) layer was spin-coated on the SiO_2 layer, baked at 180 °C for 2 min, and exposed at an acceleration voltage of 30 keV to define the patterns. After exposure, the wafer was developed in the solution of methyl isobutyl ketone (MIBK) and isopropyl alcohol (IPA) of MIBK: IPA = 1:3 for 35 s followed by 60 s in an IPA bath. After development, a 1 nm Ti adhesion layer and a 40 nm Au layer were deposited subsequently using thermal evaporation. Finally, top Au nanocross antennas were formed after a lift-off process.

ASSOCIATED CONTENT

Supporting Information

The Supporting Information is available free of charge at https://pubs.acs.org/doi/10.1021/acsnano.1c08597.

> Dimensions and reflection coefficients of the selected 4 meta-atoms; influence of the width of meta-atoms on the performance; the simulated performance of nano-QWPs with different orientations; the custom-built optical setup; supplementary simulation and experimental data for MS1, MS2, MS3, and MS4; calculated diffraction efficiencies for MS2 with the damping rate of bulk gold; and performance of designed metasurfaces under linearly polarized incidence (PDF)

AUTHOR INFORMATION

Corresponding Authors

Fei Ding − *Centre for Nano Optics, University of Southern Denmark, Odense M DK-5230, Denmark;* orcid.org/0000-0001-7362-519X; Email: feid@mci.sdu.dk

Sergey I. Bozhevolnyi − *Centre for Nano Optics, University of Southern Denmark, Odense M DK-5230, Denmark;* orcid.org/0000-0002-0393-4859; Email: seib@mci.sdu.dk

Authors

Yadong Deng − *Centre for Nano Optics, University of Southern Denmark, Odense M DK-5230, Denmark;* orcid.org/0000-0002-2405-0251

Cuo Wu − *Centre for Nano Optics, University of Southern Denmark, Odense M DK-5230, Denmark; Institute of Fundamental and Frontier Sciences, University of Electronic Science and Technology of China, Chengdu 610054, People's Republic of China;* orcid.org/0000-0001-9198-9173

Chao Meng − *Centre for Nano Optics, University of Southern Denmark, Odense M DK-5230, Denmark*

Complete contact information is available at: https://pubs.acs.org/10.1021/acsnano.1c08597

Notes

The authors declare no competing financial interest.

ACKNOWLEDGMENTS

This work was funded by the Villum Fonden (Award in Technical and Natural Sciences 2019, Grant Nos. 00022988 and 37372). C.M. acknowledges the support from the European Union's Horizon 2020 research and innovation programme under the Marie Sklodowska-Curie grant agreement No. 713694. C.W. acknowledges the support from the China Scholarship Council (Grant No. 2020023TO014).

REFERENCES

(1) Pedrotti, F. L.; Pedrotti, L. S. *Introduction to Optics*; Prentice Hall: Upper Saddle River, NJ, 1993; pp 333−371.

(2) Chen, H. T.; Taylor, A. J.; Yu, N. A Review of Metasurfaces: Physics and Applications. *Rep. Prog. Phys.* **2016**, *79*, 076401.

(3) Hsiao, H. H.; Chu, C. H.; Tsai, D. P. Fundamentals and Applications of Metasurfaces. *Small Methods* **2017**, *1*, 1600064.

(4) Luo, X. G. Subwavelength Optical Engineering with Metasurface Waves. *Adv. Opt. Mater.* **2018**, *6*, 1701201.

(5) Ding, F.; Pors, A.; Bozhevolnyi, S. I. Gradient Metasurfaces: A Review of Fundamentals and Applications. *Rep. Prog. Phys.* **2018**, *81*, 026401−026445.

(6) Capasso, F. The Future and Promise of Flat Optics: A Personal Perspective. *Nanophotonics* **2018**, *7*, 953−957.

(7) Sun, S. L.; He, Q.; Hao, J. M.; Xiao, S. Y.; Zhou, L. Electromagnetic Metasurfaces: Physics and Applications. *Adv. Opt. Photonics* **2019**, *11*, 380−479.

(8) Shaltout, A. M.; Shalaev, V. M.; Brongersma, M. L. Spatiotemporal Light Control with Active Metasurfaces. *Science* **2019**, *364*, 6441.

(9) Hao, J. M.; Yuan, Y.; Ran, L. X.; Jiang, T.; Kong, J. A.; Chan, C. T.; Zhou, L. Manipulating Electromagnetic Wave Polarizations by Anisotropic Metamaterials. *Phys. Rev. Lett.* **2007**, *99*, 063908.

(10) Pors, A.; Nielsen, M. G.; Valle, G. D.; Willatzen, M.; Albrektsen, O.; Bozhevolnyi, S. I. Plasmonic Metamaterial Wave Retarders in Reflection by Orthogonally Oriented Detuned Electrical Dipoles. *Opt. Lett.* **2011**, *36*, 1626−1628.

(11) Yu, N. F.; Aieta, F.; Genevet, P.; Kats, M. A.; Gaburro, Z.; Capasso, F. A Broadband, Background-Free Quarter-Wave Plate Based on Plasmonic Metasurfaces. *Nano Lett.* **2012**, *12*, 6328−6333.

(12) Zhao, Y.; Alù, A. Tailoring the Dispersion of Plasmonic Nanorods to Realize Broadband Optical Meta-Waveplates. *Nano Lett.* **2013**, *13*, 1086−1091.

(13) Pors, A.; Nielsen, M. G.; Bozhevolnyi, S. I. Broadband Plasmonic Half-Wave Plates in Reflection. *Opt. Lett.* **2013**, *38*, 513.

(14) Pors, A.; Bozhevolnyi, S. I. Efficient and Broadband Quarter-Wave Plates by Gap-Plasmon Resonators. *Opt. Express* **2013**, *21*, 2942−2952.

(15) Jiang, Z. H.; Lin, L.; Ma, D.; Yun, S.; Werner, D. H.; Liu, Z. W.; Mayer, T. S. Broadband and Wide Field-of-View Plasmonic Metasurface-Enabled Waveplates. *Sci. Rep.* **2015**, *4*, 7511.

(16) Cong, L. Q.; Xu, N. N.; Gu, J. Q.; Singh, R. J.; Han, J. G.; Zhang, W. L. Highly Flexible Broadband Terahertz Metamaterial Quarter-Wave Plate. *Laser Photonics Rev.* **2014**, *8*, 626−632.

(17) Jiang, S. C.; Xiong, X.; Hu, Y. S.; Hu, Y. H.; Ma, G. B.; Peng, R. W.; Sun, C.; Wang, M. Controlling the Polarization State of Light with a Dispersion-Free Metastructure. *Phys. Rev. X* **2014**, *4*, 021026.

(18) Xiao, S. Y.; Mühlenbernd, H.; Li, G. X.; Kenney, M.; Liu, F.; Zentgraf, T.; Zhang, S.; Li, J. Helicity-Preserving Omnidirectional Plasmonic Mirror. *Adv. Opt. Mater.* **2016**, *4*, 654−658.

(19) Lin, D. M.; Fan, P. Y.; Hasman, E.; Brongersma, M. L. Dielectric Gradient Metasurface Optical Elements. *Science* **2014**, *345*, 298−302.

(20) Yang, Y. M.; Wang, W. Y.; Moitra, P.; Kravchenko, I. I.; Briggs, D. P.; Valentine, J. Dielectric Meta-Reflectarray for Broadband Linear Polarization Conversion and Optical Vortex Generation. *Nano Lett.* **2014**, *14*, 1394−1399.

(21) Arbabi, A.; Horie, Y.; Bagheri, M.; Faraon, A. Dielectric Metasurfaces for Complete Control of Phase and Polarization with Subwavelength Spatial Resolution and High Transmission. *Nat. Nanotechnol.* **2015**, *10*, 937−943.

(22) Zheng, G. X.; Mühlenbernd, H.; Kenney, M.; Li, G. X.; Zentgraf, T.; Zhang, S. Metasurface Holograms Reaching 80% Efficiency. *Nat. Nanotechnol.* **2015**, *10*, 308−312.

(23) Guo, Q. H.; Schlickriede, C.; Wang, D. Y.; Liu, H. C.; Xiang, Y. J.; Zentgraf, T.; Zhang, S. Manipulation of Vector Beam Polarization with Geometric Metasurfaces. *Opt. Express* **2017**, *25*, 14300−14307.

(24) Wu, P. C.; Tsai, W. Y.; Chen, W. T.; Huang, Y. W.; Chen, T. Y.; Chen, J. W.; Liao, C. Y.; Chu, C. H.; Sun, G.; Tsai, D. P. Versatile Polarization Generation with an Aluminum Plasmonic Metasurface. *Nano Lett.* **2017**, *17*, 445−452.

(25) Balthasar Mueller, J. P.; Rubin, N. A.; Devlin, R. C.; Groever, B.; Capasso, F. Metasurface Polarization Optics: Independent Phase Control of Arbitrary Orthogonal States of Polarization. *Phys. Rev. Lett.* **2017**, *118*, 113901.

(26) Yan, L. B.; Zhu, W. M.; Karim, M. F.; Cai, H.; Gu, A. Y.; Shen, Z. X.; Chong, P. H. J.; Tsai, D. P.; Kwong, D. L.; Qiu, C. W.; Liu, A. Q. Arbitrary and Independent Polarization Control *in Situ via* a Single Metasurface. *Adv. Opt. Mater.* **2018**, *6*, 1800728.

(27) Ding, F.; Chen, Y. T.; Bozhevolnyi, S. I. Gap-Surface Plasmon Metasurfaces for Linear-Polarization Conversion, Focusing, and Beam Splitting. *Photonics Res.* **2020**, *8*, 707.

(28) Meng, C.; Tang, S. W.; Ding, F.; Bozhevolnyi, S. I. Optical Gap-Surface Plasmon Metasurfaces for Spin-Controlled Surface Plasmon Excitation and Anomalous Beam Steering. *ACS Photonics* **2020**, *7*, 1849−1856.

(29) Zhang, C.; Divitt, S.; Fan, Q. B.; Zhu, W. Q.; Agrawal, A.; Lu, Y. Q.; Xu, T.; Lezec, H. J. Low-Loss Metasurface Optics Down to the Deep Ultraviolet Region. *Light: Sci. Appl.* **2020**, *9*, 55.

(30) Li, Z. C.; Liu, W. W.; Cheng, H.; Choi, D. Y.; Chen, S. Q.; Tian, J. G. Spin-Selective Full-Dimensional Manipulation of Optical Waves with Chiral Mirror. *Adv. Mater.* **2020**, *32*, 1907983.

(31) Ding, F.; Chang, B. D.; Wei, Q. S.; Huang, L. L.; Guan, X. W.; Bozhevolnyi, S. I. Versatile Polarization Generation and Manipulation Using Dielectric Metasurfaces. *Laser Photonics Rev.* **2020**, *14*, 2000116.

(32) Chen, C.; Gao, S. L.; Song, W. G.; Li, H. M.; Zhu, S. N.; Li, T. Metasurfaces with Planar Chiral Meta-Atoms for Spin Light Manipulation. *Nano Lett.* **2021**, *21*, 1815−1821.

(33) Wang, D. Y.; Liu, T.; Zhou, Y. J.; Zheng, X. Y.; Sun, S. L.; He, Q.; Zhou, L. High-Efficiency Metadevices for Bifunctional Generations of Vectorial Optical Fields. *Nanophotonics* **2020**, *10*, 685−695.

(34) Xu, H. X.; Wang, Y. Z.; Wang, C. H.; Wang, M. Z.; Wang, S. J.; Ding, F.; Huang, Y. J.; Zhang, X. K.; Liu, H. W.; Ling, X. H.; Huang, W. Deterministic Approach to Achieve Full-Polarization Cloak. *Research* **2021**, *2021*, 6382172.

(35) Liu, M. Z.; Huo, P. C.; Zhu, W. Q.; Zhang, C.; Zhang, Si.; Song, M. W.; Zhang, S.; Zhou, Q. W.; Chen, L.; Lezec, H. J.; Agrawal, A.; Lu, Y. Q.; Xu, T. Broadband Generation of Perfect Poincaré Beams *via* Dielectric Spin-Multiplexed Metasurface. *Nat. Commun.* **2021**, *12*, 2230.

(36) Qiu, Y. C.; Tang, S. W.; Cai, T.; Xu, H. X.; Ding, F. Fundamentals and Applications of Spin-Decoupled Pancharatnam−Berry Metasurfaces. *Front. Optoelectron.* **2021**, *14*, 134−147.

(37) Ding, F.; Tang, S. W.; Bozhevolnyi, S. I. Recent Advances in Polarization-Encoded Optical Metasurfaces. *Adv. Photonics Res.* **2021**, *2*, 2000173.

(38) Cai, Z. R.; Deng, Y. D.; Wu, C.; Meng, C.; Ding, Y. T.; Bozhevolnyi, S. I.; Ding, F. Dual-Functional Optical Waveplates Based on Gap-Surface Plasmon Metasurfaces. *Adv. Opt. Mater.* **2021**, *9*, 2002253.

(39) Yuan, Y. Y.; Sun, S.; Chen, Y.; Zhang, K.; Ding, X. M.; Ratni, B.; Wu, Q.; Burokur, S. N.; Qiu, C. W. A Fully Phase-Modulated Metasurface as an Energy-Controllable Circular Polarization Router. *Sci. Adv.* **2020**, *7*, 2001437.

(40) Zhang, K.; Yuan, Y. Y.; Ding, X. M.; Li, H. Y.; Ratni, B.; Wu, Q.; Liu, J.; Burokur, S. N.; Tan, J. B. Polarization-Engineered Noninterleaved Metasurface for Integer and Fractional Orbital Angular Momentum Multiplexing. *Laser Photonics Rev.* **2021**, *15*, 2000351.

(41) Yuan, Y. Y.; Zhang, K.; Ratni, B.; Song, Q. H.; Ding, X. M.; Wu, Q.; Burokur, S. N.; Genevet, P. Independent Phase Modulation for Quadruplex Polarization Channels Enabled by Chirality-Assisted Geometric-Phase Metasurfaces. *Nat. Commun.* **2020**, *11*, 4186.

(42) Wang, D. Y.; Liu, F. F.; Liu, T.; Sun, S. L.; He, Q.; Zhou, L. Efficient Generation of Complex Vectorial Optical Fields with Metasurfaces. *Light: Sci. Appl.* **2021**, *10*, 67.

(43) Ding, F.; Yang, Y. Q.; Deshpande, R. A.; Bozhevolnyi, S. I. A Review of Gap-Surface Plasmon Metasurfaces: Fundamentals and Applications. *Nanophotonics* **2018**, *7*, 1129−1156.

(44) Johnson, P. B.; Christy, R. W. Optical Constants of the Noble Metals. *Phys. Rev. B* **1972**, *6*, 4370−4379.

(45) Li, Z. L.; Chen, C.; Guan, Z. Q.; Tao, J.; Chang, S.; Dai, Q.; Xiao, Y.; Cui, Y.; Wang, Y. Q.; Yu, S. H.; Zheng, G. X.; Zhang, S. Three-Channel Metasurfaces for Simultaneous Meta-Holography and Meta-Nanoprinting: A Single-Cell Design Approach. *Laser Photonics Rev.* **2020**, *14*, 2000032.

(46) Li, J. X.; Wang, Y. Q.; Chen, C.; Fu, R.; Zhou, Z.; Li, Z. L.; Zheng, G. X.; Yu, S. H.; Qiu, C. W.; Zhang, S. From Lingering to Rift: Metasurface Decoupling for Near- and Far-Field Functionalization. *Adv. Mater.* **2021**, *33*, 2007507.

Supporting Information

Functional Metasurface Quarter-Wave Plates for Simultaneous Polarization Conversion and Beam Steering

Yadong Deng,[1] Cuo Wu,[1,2] Chao Meng,[1] Sergey I. Bozhevolnyi,[1,*] and Fei Ding[1,*]

[1]Centre for Nano Optics, University of Southern Denmark, Campusvej 55, Odense M DK-5230, Denmark

[2]Institute of Fundamental and Frontier Sciences, University of Electronic Science and Technology of China, Chengdu 610054, People's Republic of China

[*]Corresponding author: feid@mci.sdu.dk; seib@mci.sdu.dk

Dimensions and reflection coefficients of the selected 4 meta-atoms

The dimensions of the 4 meta-atoms that function as nanoscale quarter-wave plates (nano-QWPs) and provide effective phase modulation of the reflected fields are presented in Table S1. In addition, the calculated phases and amplitudes of these 4 meta-atoms are also shown in Table S1, respectively. Due to the uneven amplitudes, the performance of beam steering will be affected, resulting in decreased efficiency and increased unwanted diffraction orders.

Table S1. Dimensions and reflection coefficients of the selected 4 meta-atoms.

No. of the meta-atom	L_x/nm	L_y/nm	φ_{xx}/deg	$\Delta\varphi$/deg	$\lvert r_{xx}\rvert$
1	92	141	45.1	89.7	0.97
2	144	167	135.4	90.0	0.76
3	164	245	224.8	90.1	0.71
4	249	82	315.2	89.7	0.92

Influence of the width of meta-atoms on the performance

If the width w of the meta-atom is decreased from 50 to 30 nm, the reflection amplitude decreases while the available resonance phase of nano-QWPs (*i.e.*, φ_{xx}) becomes larger, covering a wide range of > 315° (Figure S1a). Therefore, 8 meta-atoms that function as nano-QWPs providing the appropriate phase modulation of the reflected fields can be identified (Table S2). At the same time, elements No.4, No.5, and No.6 exhibit relatively low reflection amplitudes (< 60%), thereby seriously decreasing the efficiency of the phase gradient metasurface (Figure S2a). Specifically, the total reflectivity is decreased from 48% to 36% at the designed wavelength of 850 nm, and the unwanted 0-order diffraction becomes significant. In addition, the dimensions of these nano-QWPs are too close to be realistically fabricated with an acceptable accuracy. When the width w is increased to 70 nm, the reflection amplitude is increased, although at the expense of a rather limited phase coverage of only ~ 180°, as shown in Figure S1b. Nevertheless, the selected 2 nano-QWPs with the width of 70 nm (Table S3) can be used to replace the low-amplitude elements shown in Table S1. For instance, if the original element No.2 providing the reflection phase of 135° is replaced with the new element No.2 (w = 70 nm, L_x =152 nm, and L_y =183 nm), the total reflectivity is increased by 5% (Figure S2b).

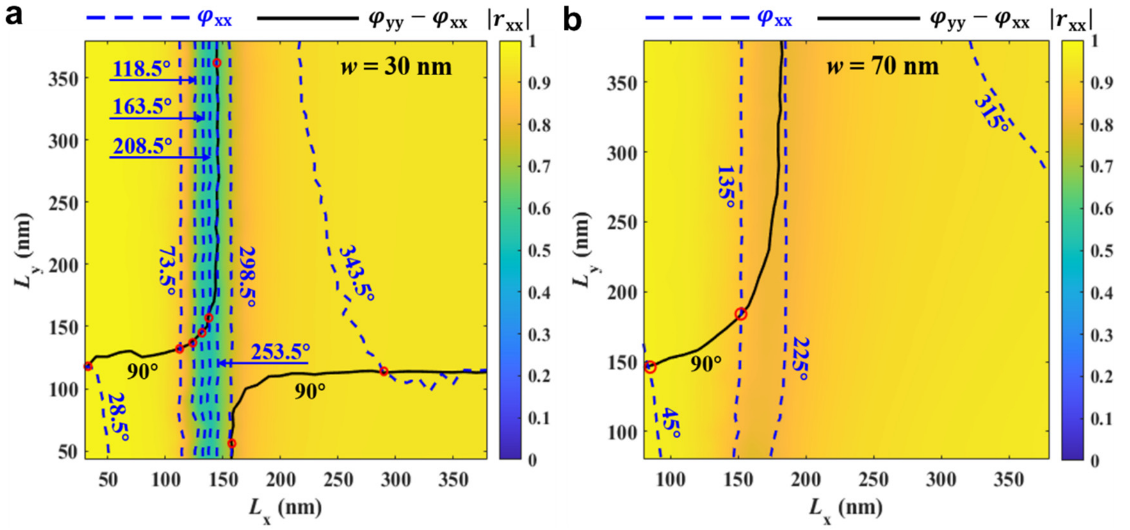

Figure S1. Calculated reflection coefficient as a function of the dimensions at the design wavelength of 850 nm for x-polarization with the width of **a)** 30 and **b)** 70 nm. The color map shows the reflection amplitude $|r_{xx}|$, while the blue dashed lines are contours of the reflection phase φ_{xx} with a step of 90° and black solid lines indicate the meta-atoms with the phase difference $\Delta\varphi = \varphi_{yy} - \varphi_{xx}$ equal to 90°. The other geometrical parameters are the same as those in Figure 1.

Table S2. Dimensions and reflection coefficients of the selected 8 meta-atoms with w = 30 nm.

No. of the meta-atom	L_x/nm	L_y/nm	φ_{xx}/deg	$\Delta\varphi$/deg	$\|r_{xx}\|$
1	33	116	28.47	89.50	0.98
2	115	132	73.52	90.68	0.86
3	126	137	118.52	89.20	0.69
4	133	145	163.57	90.58	0.54
5	139	157	208.46	90.10	0.52
6	145	362	253.43	89.83	0.57
7	154	52	298.41	90.17	0.76
8	284	114	343.52	89.97	0.94

Table S3. Dimensions and reflection coefficients of the selected 2 meta-atoms with w = 70 nm.

No. of the meta-atom	L_x/nm	L_y/nm	φ_{xx}/deg	$\Delta\varphi$/deg	$\|r_{xx}\|$
1	83	146	44.96	90.22	0.97
2	152	183	134.57	90.69	0.86

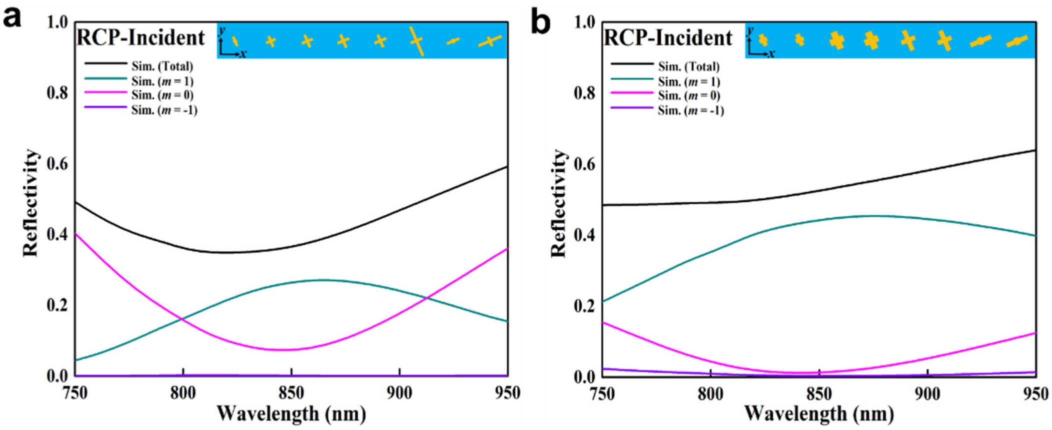

Figure S2. Simulated diffraction efficiencies of the GSP gradient MS1 for circular-to-linear polarization conversion and beam steering as a function of wavelength for RCP incident light. In **a)**, the MS1 supercell is composed of 8 elements with w = 30 nm selected from Table S2. In b), the original element No.2 (w = 50 nm, L_x = 144 nm, and L_y = 167 nm) that provides the phase of 135° is replaced with the new element No.2 (w = 70 nm, L_x = 152 nm, and L_y = 183 nm) while the other 3 elements are not changed.

The simulated performance of nano-QWPs with different orientations

Figure S3 shows the simulated degree of linear polarization (DoLP) and angle of linear polarization (AoLP) of the four designed nano-QWPs as a function of the rotation angle of θ with respect to the x-axis under RCP incident light at the wavelength of 850 nm. With the rotation angle θ changed from 0° to 90°, the DoLPs stay around 0.99 and AoLPs follow the linear distribution of $\theta + 45°$, which is consistent with the theoretical predictions in all cases. Therefore, our designed four meta-atoms are not affected by the near-field coupling between adjacent cells with respect to the nano-QWP rotation, continuing to function as excellent nano-QWPs.

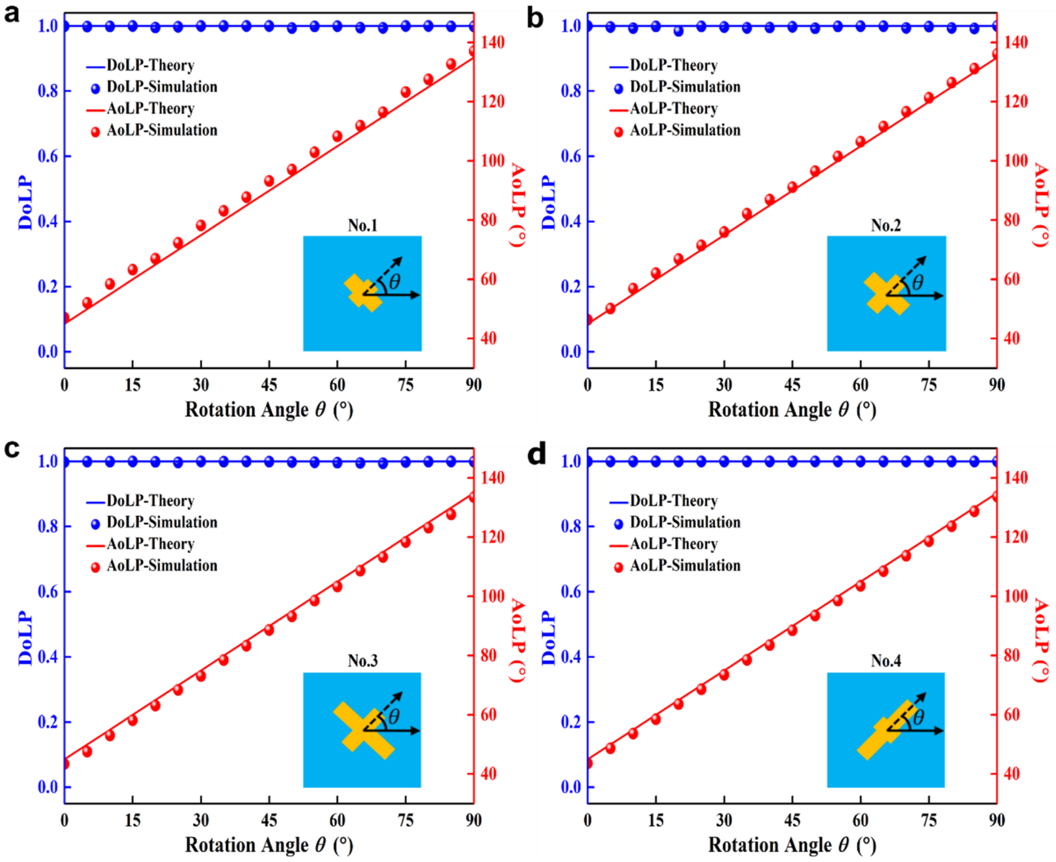

Figure S3. Calculated DoLPs and AoLPs the four designed nano-QWPs as a function of the rotation angle of θ with respect to the x-axis under RCP incident light at the wavelength of 850 nm.

The custom-built optical setup

In order to experimentally test and verify the performance of our fabricated metasurfaces, the prepared samples are characterized using a custom-built optical setup shown in Figure S4. The fiber-collimated near-infrared light from a tunable Ti: Sapphire laser (Laser, Spectra-Physics, Model 3900S) first passes through a half-wave plate (HWP, Thorlabs, AHWP05M-980) and an attenuator (Thorlabs, NE01B) to adjust the intensity of the output light. Then the output light passes through a linear polarizer (LP1, Thorlabs, LPN1R050-MP2) and a quarter-wave plate (QWP, Thorlabs, AQWP10M-980) to generate a left-handed circularly polarized (LCP) or right-handed circularly polarized (RCP) beam. Then the circularly polarized (CP) beam passes through one silver mirror (Mirror, Thorlabs, PF10-03-P01) and 2 beam splitters (BS1 and BS2, Thorlabs, CM1-BS014) which could adjust the direction of the beam propagation and compensate for the actual phase retardance caused by one single beam splitter. Then the CP beam is slightly focused on the sample with a spot size smaller than the sample area by a long working distance objective (Obj, Mitutoyo, M Plan Apo, 20×/0.42 NA). The reflected signal collected by the same objective passes through BS2, a tube lens (TL, Thorlabs, TTL200-S8, $f = 200$ mm) and then an iris (Thorlabs, ID12Z/M) that located at the first direct image plane to select a specific area of interest in the sample. The filtered first direct image is then imaged again by another relay lens (RL, Thorlabs, AC254-100-B-ML, $f = 100$ mm) onto one charge-coupled device (CCD1, Thorlabs, DCC1545M-GL). Note that another same CCD camera (CCD2) could be mounted at different positions to get Fourier images, and linear polarizer (LP2, Thorlabs, LPN1R050-MP2) is mounted between CCD2 and RL for polarization-resolved measurement. The efficiencies and polarization properties of the reflected light are measured on the Fourier plane, at which different diffraction orders are well separated in space.

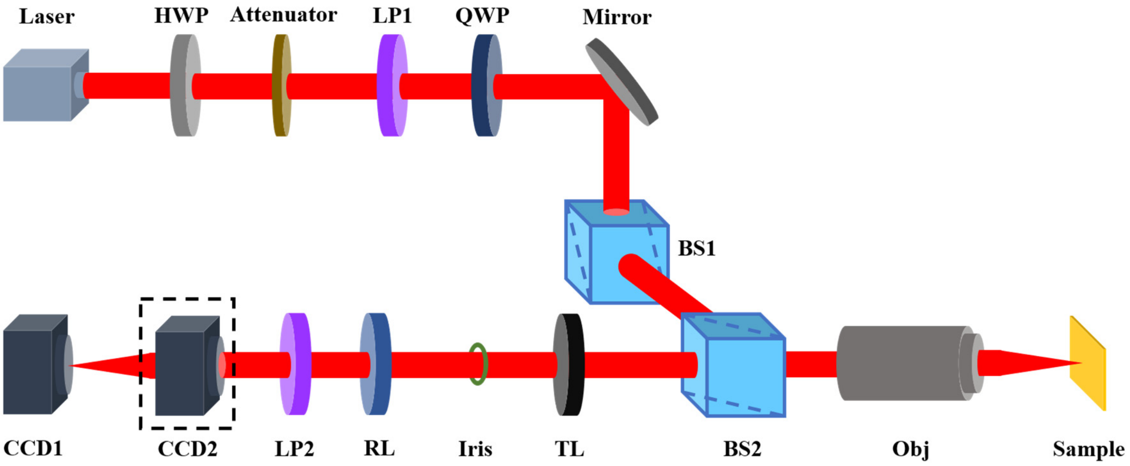

Figure S4. Schematic of the experimental setup for characterizing metasurfaces.

Supplementary simulation and experimental data for MS1

Under RCP incident light, the simulated (dark cyan solid line) and measured (dark cyan star markers) polarization state diagrams as a function of the orientation of the analyzer for +1 diffraction order at wavelengths of 800 and 900 nm are shown in Figure S5, which are in good agreement with each other. The measured degrees of linear polarization (DoLPs) are 99.56% and 99.16% at wavelengths of 800 and 900 nm, respectively, consistent with the DoLPs of 99.27% and 99.82% in the simulation.

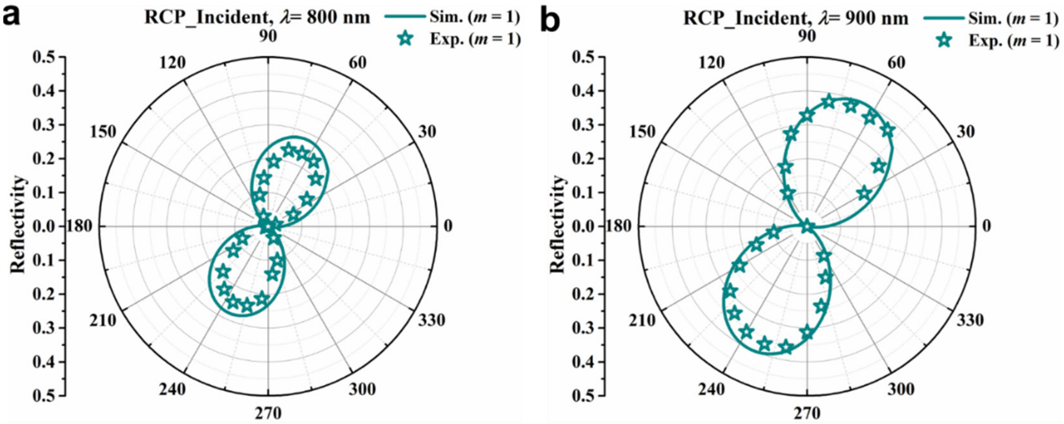

Figure S5. Simulated (dark cyan solid line) and experimental (dark cyan star markers) polarization state diagrams of the steered beam within +1 diffraction order for RCP incident light at wavelengths of **a)** 800 nm and **b)** 900 nm.

Under LCP incident light, we include related simulations and measurements in Figure S6. Figure S6a compares the simulated (four colorful solid lines) and measured (colorful markers) diffraction efficiencies of different diffraction orders from $m = -1$ to +1 as a function of wavelength. In general, the simulated and measured diffraction efficiencies coincide fairly well. At the design wavelength of 850 nm, almost all the incident energy has been reflected to +1 diffraction order, demonstrate the excellent capability of steering. Quantitatively, the total measured reflected efficiency is 47.60% (simulated value is 50.20%) and the +1-order diffraction efficiency is 36.50% (simulated value is 40.00%) at $\lambda = 850$ nm. As shown in Figure S6b-S6d, there is a reasonable agreement between the measured and simulated efficiencies at different diffraction orders: the measured DoLPs (orange star markers) are 99.15%, 99.70%, and 99.71% at wavelengths of 800, 850, and 900 nm, respectively, and the simulated DoLPs (orange solid lines) are 99.82%, 99.13% and 99.36% at wavelengths of 800, 850, and 900 nm, respectively.

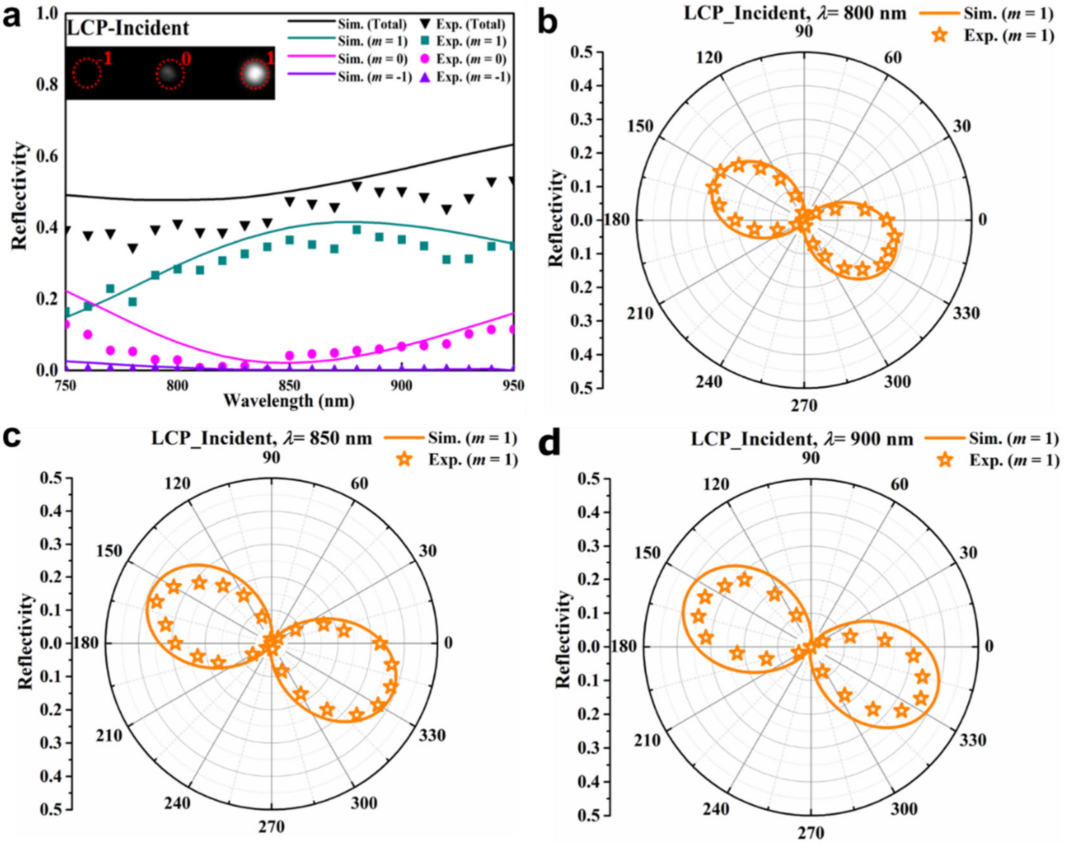

Figure S6. a) Simulated (solid lines) and experimental (markers) diffraction efficiencies of different orders as a function of wavelength for LCP incident light. The inset shows the optical image of the diffraction spots at the wavelength of 850 nm. Simulated (orange solid line) and measured (orange star markers) polarization state diagrams of the steered beam within +1 diffraction order for LCP incident light at wavelengths of **b)** 800 nm, **c)** 850 nm and **d)** 900 nm.

Supplementary simulation and experimental data for MS2

The simulated (dark cyan/violet solid line) and measured (dark cyan/violet star markers) polarization state diagrams as a function of the orientation of the analyzer for ±1 diffraction order at wavelengths of 800 and 900 nm under RCP excitation are shown in Figure S7. From Figure S7, it is clear that there is a good agreement between the simulated and measured DoLPs for different diffraction orders. At λ = 800 nm, the measured (simulated) DoLPs are 99.45% (99.19%) and 99.52% (99.32%) for diffraction orders of $m = \pm 1$, respectively. At λ = 900 nm, the measured (simulated) DoLPs are 99.40% (99.50%) and 99.10% (99.52%) for diffraction orders of $m = \pm 1$, respectively.

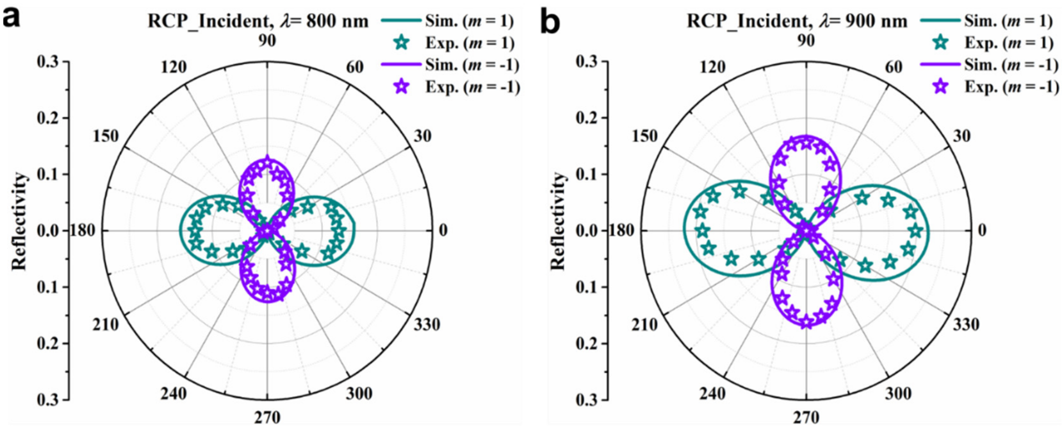

Figure S7. Simulated (dark cyan/violet solid line) and experimental (dark cyan/violet star markers) polarization state diagrams of the steered beams within ±1 diffraction orders for RCP incident light at wavelengths of **a)** 800 nm and **b)** 900 nm.

Under LCP incident light, the simulated (four colorful solid lines) and measured (colorful markers) diffraction efficiencies are well-matched with each other in Figure S8a. In particular, the diffraction efficiency of +1 order is 20.80% (simulated value is 23.00%) and the diffraction efficiency of −1 order is 17.00% (simulated value is 19.30%) at λ = 850 nm. As shown in Figure S8b-S8d, there is a reasonable agreement between the measured and simulated efficiencies at different diffraction orders: the measured DoLPs (orange/purple star markers) are 99.06%, 99.30%, and 99.26% for the +1 diffraction order and 99.10%, 99.61%, and 99.31% for the −1 diffraction order at wavelengths of 800, 850, and 900 nm, respectively; the simulated DoLPs (orange/purple solid line) are 99.73%, 99.65%, and 99.44% for the +1 diffraction order and 99.62%, 99.35%, and 99.41% for the −1 diffraction order at wavelengths of 800, 850, and 900 nm, respectively.

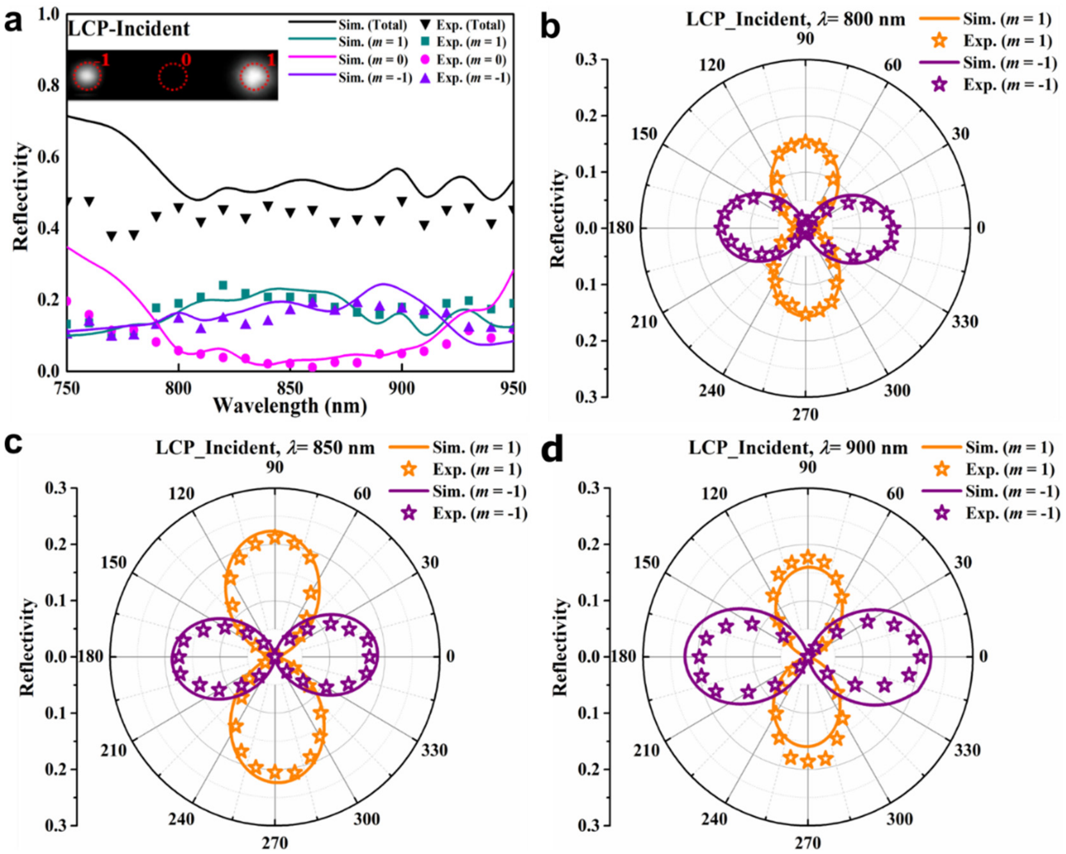

Figure S8. a) Simulated (solid lines) and experimental (markers) diffraction efficiencies of different orders as a function of wavelength for LCP incident light. The inset shows the optical image of the diffraction spots at the wavelength of 850 nm. Simulated (orange/purple solid line) and measured (orange/purple star markers) polarization state diagrams of the steered beams within ±1 diffraction orders for LCP incident light at wavelengths of **b)** 800, **c)** 850, and **d)** 900 nm.

Supplementary simulation and experimental data for MS3

To show the capability of steering co- and cross-polarized CP channels, we plot the electric field distributions of the reflection light for diffraction orders of $m = 0$ (Figure S9a) and 1 (Figure S9c) at the design wavelength of 850 nm for RCP incident light, which indicate the well-defined wavefronts. Figure S9b and S9d display the simulated (dark cyan/ magenta solid line) and experimental (dark cyan/ magenta star markers) polarization state diagrams as a function of the orientation of the analyzer at λ = 800 and 900 nm, manifesting reasonable agreements. Specifically, the measured degrees of circular polarization (DoCPs) (dark cyan/ magenta star markers) are 90.60% and 91.10% for 0 diffraction order and −93.40% and −90.70% for +1 diffraction order at wavelengths of 800 and 900 nm, respectively, which are a little lower than the simulated values (dark cyan/ magenta solid line) of 99.35% and 99.41% for 0 diffraction order and −99.44% and −99.65% for +1 diffraction order at λ = 800 and 900 nm, respectively.

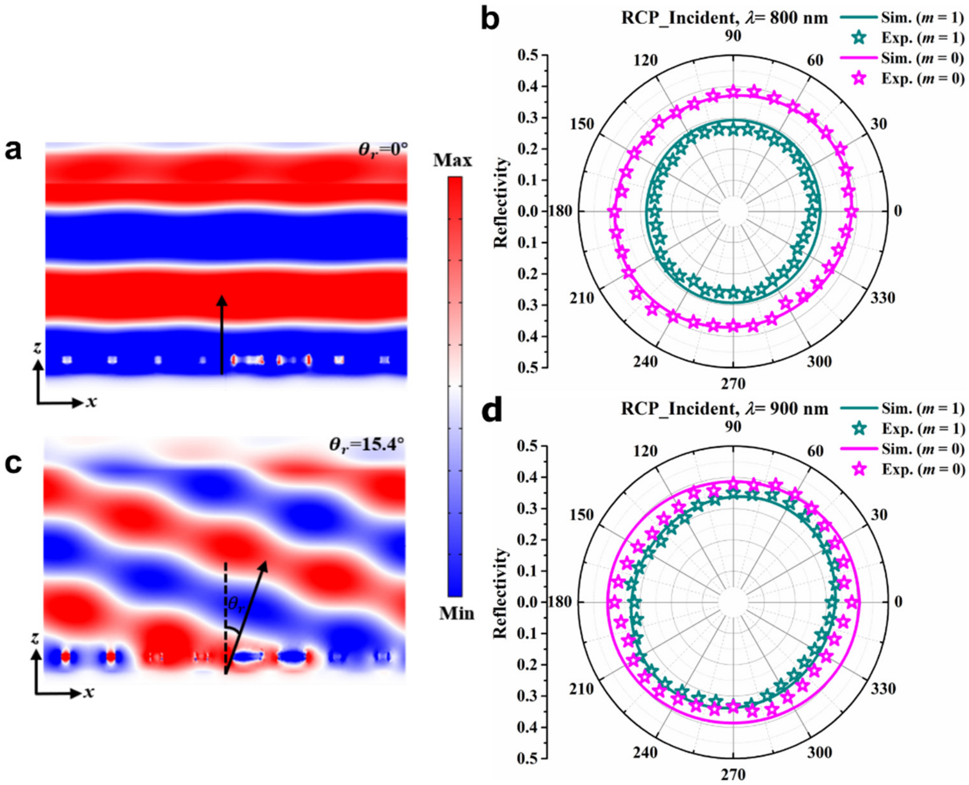

Figure S9. Electric field distributions of the reflection light for diffraction orders of **a)** $m = 0$ and **c)** $m = 1$ of MS3 at the design wavelength of 850 nm under RCP excitation. Simulated (dark cyan/magenta solid line) and experimental (dark cyan/magenta star markers) polarization state diagrams as a function of the orientation of the analyzer for RCP incident light at wavelengths of **b)** 800 and **d)** 900 nm.

Supplementary simulation and experimental data for MS4

For MS4, we also plot the electric field distributions of the reflection light for diffraction orders of m = −1 and 1 at λ = 850 nm under RCP excitation, where the well-defined titled planar wavefronts can be clearly seen (Figure S10a and S10c). To verify the polarization state, the simulated (dark cyan/violet solid line) and experimental (dark cyan/violet star markers) polarization polar diagram as a function of the orientation of the analyzer at wavelengths of 800 and 900 nm are shown in Figure S10b and S10d, respectively. Generally, there is a reasonable agreement between the measured and simulated efficiencies at different diffraction orders, albeit with some discrepancies regarding the DoCPs. The measured DoCPs (dark cyan/ violet star markers) are 90.24% and 92.40% for −1 diffraction order and –90.10% and −89.30% for +1 diffraction order at λ = 800 and 900 nm, respectively, while the simulated DoCPs (dark cyan/ violet solid line) are 99.66% and 99.89% for −1 diffraction order and −99.60% and −99.65% for +1 diffraction order at wavelengths of 800 and 900 nm, respectively.

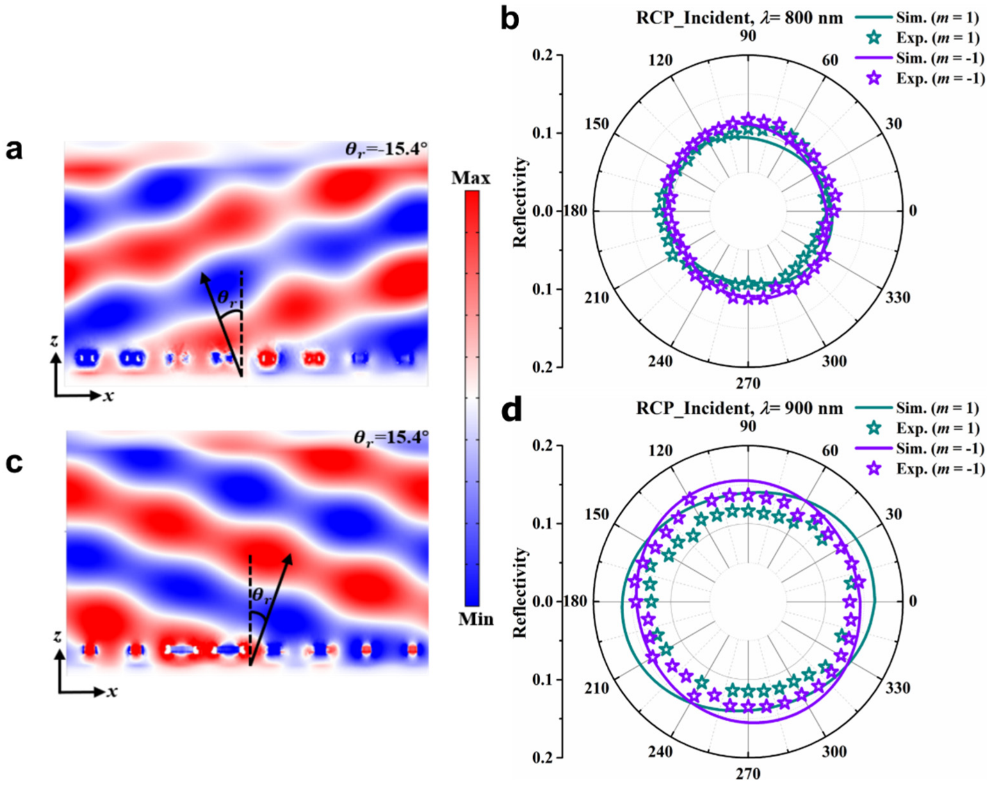

Figure S10. Electric field distributions of the reflection light for diffraction orders of **a)** m = 0 and **c)** m = 1 of MS4 at the design wavelength of 850 nm under RCP excitation. Simulated (dark cyan/magenta solid line) and experimental (dark cyan/magenta star markers) polarization state diagrams as a function of the orientation of the analyzer for RCP incident light at wavelengths of **b)** 800 and **d)** 900 nm.

Calculated diffraction efficiencies for MS2 with the damping rate of bulk gold

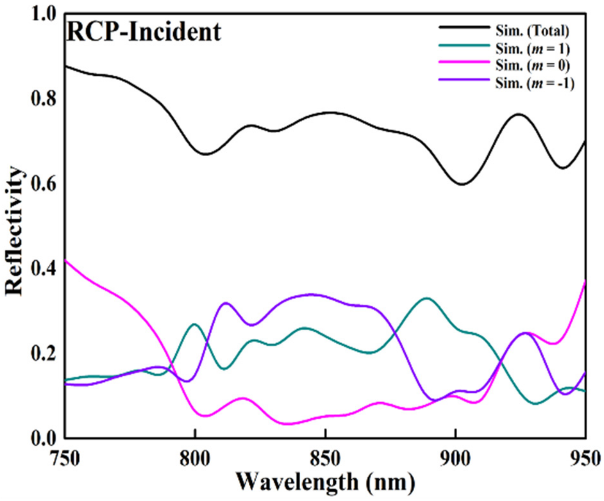

Figure S11. Simulated diffraction efficiencies of different orders as a function of wavelength for MS2 under the RCP excitation. The damping rate of Au meta-atoms is the same as that of bulk gold.

Performance of designed metasurfaces under linearly polarized incidence

Table S4 summaries the polarization states of reflected light within different diffraction orders for the designed four metasurfaces (MS1 to MS4) under a linearly polarized (LP) excitation at the designed wave length of 850 nm.

Table S4. Performance of designed metasurfaces under linearly polarized incidence

	Input (LP, AoLP)	Output ($m = -1$)	Output ($m = 0$)	Output ($m = 1$)
MS1	67.5°	×	×	RCP
	−22.5°			LCP
MS2	0°	LCP	×	RCP
	90°	RCP		LCP
MS3	0°	RCP	LP (0°)	LCP
	90°	RCP	LP (0°)	LCP
MS4	0°	LP (0°)	×	LP (30°)
	90°	LP (90°)		LP (120°)